

Carbon-Coated Nanopowder as Sintering Aid for Water-Atomized Iron Powder

Swathi Kiranmayee Manchili (✉ manchili@chalmers.se)

Chalmers University of Technology

Fang Liu

Chalmers University of Technology

Eduard Hryha

Chalmers University of Technology

Lars Nyborg

Chalmers University of Technology

Research Article

Keywords: sintering, carbon-coated nanopowder, nanopowder, X-ray photoelectron spectroscopy, HR TEM, thermogravimetry

Posted Date: January 7th, 2022

DOI: <https://doi.org/10.21203/rs.3.rs-1220313/v1>

License: © ⓘ This work is licensed under a Creative Commons Attribution 4.0 International License.

[Read Full License](#)

Abstract

The influence of carbon coating on the nanopowder when used as a sintering aid for water-atomized iron powder is explored. Iron nanopowder without such a coating was used as a reference sintering aid to isolate and depict the influence of the carbon coating. Both nanopowder variants were characterized using XPS and HRTEM, and the results showed a core-shell structure for both nanopowder variants. Iron nanopowder is covered by a 3-4 nm thick iron oxide layer, while the carbon-coated nanopowder is encapsulated with a number of nanometric carbon layers. Thermogravimetry carried out in a pure hydrogen environment shows a multippeak behaviour for carbon-coated nanopowder, while a single peak behaviour is observed for the iron nanopowder. This difference was correlated with chemical analysis. Two types of micro/nanobimodal powders were obtained by mixing the nanopowder with water-atomized iron powder. An improved linear shrinkage was observed when carbon-coated iron nanopowder was added. This can be explained by the reduced surface diffusion in the nanopowder due to the carbon coating, which allows the nanopowder to sinter at higher temperatures and improves densification.

Introduction

Press and sinter is a powder metallurgical (PM) manufacturing route in which metal powder is processed through shaping processes such as uniaxial compaction to the required shape, and then the compact material is sintered to make it useful for application. During sintering, the part is heated so that the metal particles bond to each other, which imparts the required strength. The strength obtained is proportional to the density of the component ¹. Hence, it is essential to improve density to improve properties and subsequently widen the range of applications of PM components. There are many ways through which density could be improved. One of the ways is to add a sintering aid, and nanopowder is one such possible sintering aid, which is known to lower the activation energy needed for sintering ^{2,3}. The addition of nanopowder has been explored in the field of metal injection moulding (MIM), where enhanced properties were observed ⁴.

Nanoparticles have unique size-dependent properties, attributed to the large fraction of atoms present at the surface in comparison to their counterbulk materials ^{5,6}. These unique properties have already been exploited for applications in areas such as chemical analysis, microelectronics, biological sensors and other functional applications ^{7,8}. However, for nanoparticles to be useful in these applications, it is important that they remain stable and retain their size. Because of their large surface-to-volume ratio, there is excess surface energy associated with them. Therefore, there is a strong tendency to coalesce, which leads to significant changes in processability. Carbon can be coated onto nanopowder, which stabilizes the nanoparticles against agglomeration/coalescence. Carbon-coated iron nanopowder has been actively used for applications such as magnetic data storage, magnetic toners in xerography, contrast agents in magnetic resonance imaging, catalyst supports and drug and gene delivery systems ⁹. Additionally, having carbon-coated nanopowder would constitute a source for carbon, which otherwise would need to be added separately to set the indented final composition of the sintered steel.

In previous work, the authors explored the addition of pure iron nanopowder as a sintering aid to water-atomized iron powder¹⁰. The sinter curves revealed a pronounced influence of nanopowder addition on the sintering behaviour of these micro/nano bimodal powder compacts. Sintering experiments at intermittent temperatures to follow the development of sinter necks with increasing temperature and subsequent fractographic analysis of the compacts revealed that the sintering of nanopowder at temperatures as low as 600°C, below the onset of the sintering of the micrometre-sized base powder. In this study, the possibility of utilizing carbon-coated iron nanopowder as a sintering aid instead of pure iron nanopowder is being explored. The primary objective is to determine how the presence of carbon on the surface of iron nanopowder influences the sintering of water-atomized iron powder. For this purpose, two systems have been selected: one having carbon-coated iron nanopowder and the other nanopowder without any such coating. The base powder in both cases is micrometre-sized water-atomized iron powder. A detailed characterization of both kinds of nanopowders using X-ray photoelectron spectroscopy and high-resolution transmission electron microscopy was carried out. A comparison in terms of sinterability was performed between the two variants of micro/nano bimodal powder compacts.

Results And Discussion

XPS of nanopowder

X-ray photoelectron spectroscopy (XPS) measurements were performed to investigate the surface chemical characteristics of both Fe NPs and CC NPs. Figure 1 shows the survey spectra of both Fe NPs and CC NPs along with the high-resolution spectra for carbon (C1 s) and iron (Fe2p^{3/2}). The survey scan of both nanopowders with binding energies from 0 to 1100 eV carried out on the as-prepared sample surface shows the elements present in the near surface region of the powder, as shown in Figure 1a. The spectra reflect the presence of iron, oxygen and carbon indicated by their characteristic peaks.

The high-resolution XPS results provide a better understanding of the surface characteristics of the nanopowder variants. Figure 1b shows the different peak positions for carbon (C1 s) for the two nanopowder variants. The C1 s peak position for the carbon-coated nanopowder is 284.4 eV, while it is 285.2 eV for the iron nanopowder. These positions correspond to graphitic carbon and carbonaceous contamination layers on the two kinds of nanopowders, respectively^{11 12}. The high-resolution XPS spectra of iron (Fe2p^{3/2} region) in Figure 1c show both strong iron oxide peaks but different relative intensities for metallic iron. The highest relative amount of metallic iron is indicated for the carbon-coated nanopowder. Now, from the relative intensities of the iron oxide and metallic iron peaks, the overall oxide thickness can be depicted, as XPS is sensitive to the outer 3 to 5 nm of a sample, as the signal comes from a maximum of three times the attenuation length of the photoelectrons¹³. In a previous study, a detailed assessment of the oxide layer thickness was carried out involving the application of different models/approaches, and it was found that the thickness of the oxide scale on Fe NPs is approximately 3 nm¹⁴. Now, to understand the difference in the surface chemical structure of the two variants in more detail and in particular, the XPS results are complemented with HR TEM.

High resolution transmission electron microscopy

Figure 2 shows the TEM images of both nanopowders, revealing the characteristics with respect to shape, size and surface structure. Figure 2a shows the TEM image of Fe NPs at low magnification illustrating several particles. The size of the particles is less than 100 nm. The nanopowder is observed to be spherical. The high-resolution micrographs in Figure 2b-c show that the particle fits the core-shell model and that the oxide shell is 3-4 nm thick. This validates the XPS studies carried out on the same powder by authors elsewhere.

Figure 2d shows several particles of CC NPs at low magnification. Similar to Fe NPs, CC NPs were less than 100 nm in size and had a spherical morphology. The structure of the carbon layer surrounding the nanopowder was investigated using the HRTEM technique, and the corresponding results are shown in Figure 2e-f. The presence of a multilayer carbon coating, which is compact and adherent on the iron particles, can be noted. The iron core is entirely coated by a multilayer carbon shell, which is an indication of an integrated core-shell structure. The interplanar spacing is measured to be approximately 0.30-0.35 nm, which is similar to the value for graphite⁹. The fact that the carbon shell appears to tightly cover the nanoparticles means that both the iron oxide and metallic iron peaks detected by XPS for this powder must come from the core below and that their relative intensities reflect the different damping below the carbon shell. Additionally, it can be said that the carbon shell imposes much less damping of the XPS signals from the core than an oxide layer, and the actual oxide layer (presumably located as an interface compound) must be much thinner than in the case of the iron nanopowder.

Thermal analysis

Figure 3a shows the thermogravimetric graphs for micrometre-sized reference powder (ASC 300) and the micro/nano bimodal powder with the two different variants of nanopowder. The change in mass is recorded as a function of temperature in pure hydrogen. The mass loss when nanopowder was added was much higher than that without such an addition. Figure 3b shows the change in the mass of Fe NPs and CC NPs and the mass loss rate as a function of temperature under the same conditions. The total mass loss is 5.6% and 10% for the Fe NPs and CC NPs, respectively. In the case of Fe NPs, the mass loss can be attributed to oxygen removal through the reduction of surface oxides in a single step. The surface oxide (Figure 2) is reduced at temperatures below 500°C, above which the change in mass is negligible. The rate of change in mass, which is the first derivative, as shown in Figure 3b, shows a single peak at 355°C, indicating the temperature of the maximum reduction rate. The mass change is observed over a narrow range of temperatures. A detailed study regarding the reduction behavior and kinetics of Fe NPs is found elsewhere¹⁵, which clearly points to the existence of a single reduction step. The CC NPs show a mass loss of approximately 10%, and this mass loss is shown over a temperature range of between 300 and 700°C. Although the change in mass loss appears to be a single step, the derivative shows at least 4 peaks at 275, 383, 475 and 558°C. The mass loss is hence suggested to be attributed to both reduction by hydrogen at lower temperature and that related to the action of carbon. Figure 3a shows that the total mass losses observed were 0.15, 0.34 and 0.59% for the ASC 300, ASC+Fe NP and ASC+CC NP powders,

respectively. The difference in total mass loss is supposed to be attributed to oxygen removal from the nanopowder. The mass loss was higher in the case of ASC+CC NPs than in the case of ASC+Fe NPs. A total mass loss of 0.34% was observed for the ASC+Fe NPs, while an increased mass loss of 0.59% was shown for the ASC+CC NPs. For ease of understanding, the TG curve can be divided into two different regions. Region one corresponds to the temperature range of below 500°C, where the mass loss is related to the surface oxide reduction for both the NP variants and ASC 300. Above this temperature, there is the second temperature range, during which reduction of more stable particulate oxides predominantly found on the base powder and potential internal oxides takes place. The reduction of particulate oxides at higher temperatures has been studied in detail elsewhere^{16 17}. Nevertheless, the major fraction of the total mass loss corresponds to the first region. The increase in the mass loss between ASC 300 and the micro/nano bimodal powder is hence attributed to the reduction of surface oxide present in the nanopowder. The increase in mass loss in the case of CC NPs is connected to the loss of both oxygen and carbon, where the latter is consumed for carbothermal reduction of oxides at elevated temperatures. Hence, the added carbon via the CC NPs will also play a role in the reduction of the particulate oxides, as this will not take place to the same extent when sintering ASC 300 only in the present case, as no graphite is added here.

Chemical analysis

Table 1 shows the carbon and oxygen levels for the different powder variants and mixes and their sintered conditions. The carbon content of the ASC 300 powder was 0.005 wt.%, whereas the carbon content of the Fe NPs was less than 0.1 wt.%; therefore, the total carbon content in the ASC+Fe NP mix is supposed to be a maximum of 0.006 wt.%. When sintered under a pure hydrogen environment, this reduced to negligible 0.002 wt.%. Consequently, approximately 2/3rd of the carbon is utilized during sintering, as carbon is the predominant reducing agent at elevated temperatures¹⁸. Hence, it is suggested that this carbon loss is a result of the reduction of particulate oxides at higher temperatures through carbothermal reactions.

In the ASC+Fe NP powder, most of the oxygen content is contributed by the surface oxide present on the Fe NPs. When Fe NPs were added to ASC 300, the oxygen content increased from 0.1 to 0.28 wt.%, which is an approximately threefold increase. The 3 nm thick surface oxide on the Fe NPs sums up to 5.5 wt.% oxygen content in the Fe NPs. Upon sintering, the oxygen content was reduced to 0.02 wt.% in the ASC+Fe NP compact, which accounted for only 7% of the total oxygen content. The remaining 93%, present to a large extent in the form of iron oxide on the surface of Fe NPs and iron-rich surface oxides and possibly some particulate oxides present in ASC 300, was reduced during the course of sintering.

For the CC NPs, the carbon content was found to be 4.7 wt.%. When added to ASC 300, the total carbon content was supposed to be 0.24 wt%, which is two orders of magnitude higher than that of ASC+Fe NPs. When sintered, the carbon content was reduced to 0.01 wt. %. This means that only 6% of the total carbon remained after sintering. The remaining 94% was utilized in the reduction of oxides. The oxygen content in CC NP was 7.5 wt.%. When mixed with ASC 300, the powder mix has 0.37 wt.% oxygen. Upon sintering,

97% of the total oxygen content was reduced, as only 0.013 wt.% remained. Consequently, carbon added via the nanopowder is highly active and directly involved in surface oxide reduction and supposedly contributes to the overall reduction of all surface oxides in the material, hence significant carbon loss and extremely efficient reduction. The final level of oxygen of approximately 0.01 wt% is well below what is observed in conventional press and sinter material sintered at 1250 °C.

Table 1
Carbon and oxygen values before and after sintering

Material	Carbon, wt.%	Oxygen, wt.%
Fe NP, powder	0.06	5.5
CC NP, powder	4.7	7.5
ASC 300+Fe NP, powder	0.006	0.28
ASC 300+CC NP, powder	0.24	0.37
ASC 300+Fe NP, sintered	0.002	0.02
ASC 300+CC NP, sintered	0.014	0.013

Sintering

Compacts of ASC 300 and ASC 300 mixed with the different variants of nanopowder at a ratio of 95:5 were subjected to sintering runs in a dilatometer (DIL). In addition to the sintering shrinkage, the materials undergo dimensional changes associated with thermal expansion, allotropic transformations and events that lead to the development of their microstructure during heating and cooling. Figure 4 shows the sintering curves for the compacts sintered at 1250°C when heated at 10°C/min, isothermally held for 60 min and cooled at 30°C/min. It should be noted that all three compacts were sintered under identical sintering conditions. During the runs in DIL, the change in the linear dimension is measured as a function of time and temperature. The curve can be divided into three different stages: heating, isothermal holding and cooling. During the heating stage, the material expands, and the slope of the curve gives the coefficient of thermal expansion. In addition, sintering can take place during the heating stage, which can be seen as a deviation from the expected expansion. During isothermal holding, the compact undergoes shrinkage depending on the sinterability of the material. Then, during the cooling stage, the compactness is expected to shrink. Dimensional changes are also subjected to phase transformations. In this case, similar to typical iron systems, the transformation from body-centered cubic (BCC) ferrite to face-centered cubic (FCC) ferrite occurs during the heating stage.

The linear shrinkage values are 1, 1.3 and 2.6% for the ASC 300, ASC+Fe NP and ASC+CC NP sintered compacts, respectively. There is hence a clear difference in the sintering behaviour between the compact without and with nanopowder. This difference, observed in the low temperature regime, has been studied by the authors in detail elsewhere ¹⁰. The change in slope of the sinter curves during both heating and

cooling at approximately 900°C for the ASC and ASC+Fe NP compacts and at lower temperatures for the ASC+CC NP compact can be explained by the phase transformations taking place. For the ASC 300 and ASC+Fe NP compacts, the BCC to FCC transformation occurred at ~912°C, as expected for pure iron. It should be noted that the carbon content in ASC 300 and ASC+Fe NP powder was 0.005 and 0.006 wt.%

An improved linear shrinkage was observed in the case of the ASC+CC NP compact compared to the ASC + Fe NP compact. The HRTEM results clearly show a coating of graphitic carbon over the whole iron particle. Research has shown that the carbon present on the surface of nanoparticles serves as a barrier to the sintering of nanoparticles⁶. The surface diffusivity of silver in the presence of carbon coating was, for example, assessed by using in situ HRTEM techniques, and it was found that it is several orders of magnitude lower than the values obtained from bulk silver at high temperatures and when extrapolated to room temperature. From the experiments in ref. [2], it was suggested that as the surface of silver nanoparticles is carbon-coated, the diffusion of atoms from the surface to the neck occurs through the carbon layer. As the neck grows, the carbon coating is pushed outwards from the neck region to drive further growth. This process is slower than the surface diffusion of pure silver, which results in lower initial diffusivity values in the presence of carbon. In the present case, a thin iron oxide layer is sandwiched between the carbon coating and the iron core for CC NPs, as postulated from the XPS and HRTEM analyses performed. During the heating cycle, the iron oxide is expected to be reduced for the sintering to proceed in the lower temperature regime for the NPs. However, in the case of CC NPs, the carbon coating is expected to hinder the reduction process by hydrogen along with lowering the surface diffusivity of the iron. This would lead to reduced sintering of the nanopowder in the low-temperature regime, contrary to what is expected in nanopowder-added sintering. The sintering is then activated once the carbothermal reduction of the sandwiched oxide is possible as the temperature is raised. Consequently, hydrogen is tentatively not as active to reduce this sandwiched oxide layer of the CC NPs as long as the carbon layer is intact.

Density

Comparing the green and sintered density data, shown in Figure 5, for both compacts with added nanopowder, it was observed that ASC+CC NPs had a slightly higher green density than the ASC+Fe NP compact. The relative density for the ASC+Fe NP green compact was 0.78, whereas for the ASC+CC NP green compact, it was 0.79. Regarding the sintered density, this followed the same trend as the green density; namely, the compact ASC+CC NPs had a higher final sintered density than that of the ASC+Fe NPs. The relative densities for the final sintered compacts were 0.81 and 0.83 for ASC+Fe NP and ASC+CC NP, respectively. Since the green densities were slightly different between the two compacts, the densification parameter can be used to evaluate the effect of each nanopowder on sintering. The densification parameter is defined as the change in density during sintering divided by the change needed to attain a pore-free solid¹⁹. It is given by the following equation:

$$\psi = \frac{\rho_s - \rho_g}{1 - \rho_g} \quad (1)$$

where ρ_s is the sintered density and ρ_g is the green density. The theoretical density of iron is now considered to be 7.9 g/cc. The densification parameter is then found to be 0.2 for ASC+CC NP and 0.13 for ASC+Fe NP sintered compacts. The densification of the compacts containing CC NPs was hence greater than that of the compacts containing Fe NPs. Even if closed porosity is not reached, the higher densification parameter of the compact with CC NP points to the fact that there could be a potential effect of shifting the densification towards more closed porosity taking advantage of, in particular, the effect of carbon coating.

Microstructure of sintered compacts

Figure 6 shows the microstructure of both ASC+Fe NP and ASC+CC NP sintered compacts. Figure 6a reveals ferrite grains in ASC+Fe NP sintered compact, while Figure 6b shows a combination of ferrite and pearlite in ASC+CC NP sintered compact. The total volume fraction of pearlite is lower, and Figure 6b shows the region where pearlite is present. Using the Trainable Weka Segmentation tool, part of Fiji ImageJ freeware, the volume fraction of pearlite was estimated to be 2%. The percentage of carbon needed for 2% pearlite is supposed to be 0.05 wt.% from JMatPro calculations. Based on chemical analysis, it was established that the total carbon content after sintering of the ASC+CC NP compact was 0.014 wt.%. Pearlite pockets are hence suggested to form in the regions where the remains of carbon left after sintering are present. It should be noted that the carbon is not uniformly distributed throughout the compact and is expected to be present in the regions where nanopowder would have been present during the sintering cycle. Clearly, it is important that the carbon loss is accounted for when choosing and setting the amount of sintering aid.

Hardness of sintered compacts

Figure 7 shows the apparent hardness measured at 1 kg for the sintered compacts of ASC+Fe NPs and ASC+CC NPs. The hardness value of ASC+Fe NP sintered compact was 33 HV in line with expected for pure iron, while ASC+CC NP sintered compact was 42 HV owing to the finite amount of pearlite.

Carbon-coated iron nanopowder as a sintering aid for water-atomized iron powder was explored and compared with uncoated nanopowder as a sintering aid. Both nanopowder variants revealed a core-shell structure, where the iron nanopowder was composed of an iron core and oxide shell with a thickness of 3-4 nm, while the carbon-coated iron nanopowder had a graphitic carbon shell of similar total thickness with a sandwiched potentially thinner iron oxide layer between the carbon shell and the iron core.

Thermogravimetry in conjunction with chemical analysis helped in understanding the behaviour of the nanopowder with respect to oxide reduction and sintering and the effect of adding nanopowder of either variant to micrometre-sized base powder. Generally, adding nanopowder to micrometer-sized powder strongly reduces the compressibility. However, changing from iron nanopowder to carbon-coated powder provided marginally better compressibility when comparing these two variants. Improved linear shrinkage of compacts during sintering was observed with the addition of both kinds of nanopowder to micrometre-sized powder, particularly when having the carbon-coated variant. The carbon coating may inhibit the sintering enhancement by nanopowder at lower temperatures, while this becomes activated at higher

temperatures as the carbon takes part in the oxide reduction reactions. With the addition of carbon-coated nanopowder to the micrometer-sized base powder at a ratio of 5:95, an initial total carbon level of 0.24% was achieved. However, more than 90% of this total carbon is lost during sintering. The remaining carbon results in the local formation of pearlite islands, which is consistent with the slightly higher hardness for the sintered compacts with carbon-coated nanopowder in comparison to that of the iron nanopowder containing sintered compacts. In conclusion, it can be said that the carbon-coated iron nanopowder addition improved both the green and sintered density of water-atomized iron powder in comparison to that of iron nanopowder addition.

Materials And Methods

Materials

Pure iron nanopowder (Fe NP) and carbon-coated nanopowder (CC NP) were procured from Sigma–Aldrich. The particle size of both grades of nanopowder was below 100 nm. A micrometre-sized powder of pure iron, henceforth called ASC 300, with a D_{50} of 30 μm was supplied by Höganäs AB. The micrometer-sized powder and nanopowder were mixed at a ratio of 95 to 5 wt.%, yielding two variants of micro/nanobimodal powder, ASC 300+5 wt.% Fe NPs and ASC 300+5 wt.% CC NPs. Mixing was carried out in a tumbler placed in a glove box for a few hours. Storage and handling of the nanopowder was performed in a nitrogen-filled glovebox prior to any processing, sample preparation or characterization.

X-ray photoelectron spectroscopy

X-ray photoelectron spectroscopy (XPS) was carried out on both nanopowder variants using a PHI Versaprobe III equipped with a monochromatic Al K_{α} (1486.6 eV) X-ray source. Ultrahigh vacuum conditions of 10^{-9} mbar were maintained during the powder analysis. The sample surface and the X-ray beam are placed perpendicular to one another, whereas the take-off angle is 45° with respect to the sample surface. A pass energy of 140 eV was used for survey scans and 26 eV for high-resolution scans. Before the commencement of measurements, energy calibrations were carried out using pure elemental standards of gold, silver and copper. A graphite standard sample was used for the exact peak position. The binding energies were referenced to the graphitic sp_2 hybridized carbon for C1 s set at 284.4 eV^{11 20}. Samples for XPS analysis were prepared inside the glove box. Loose powder was pressed between aluminum plates, and the plate was mounted on the sample holder. The XPS data were analysed using MultiPak V9.0 software supplied with the instrument.

Transmission electron microscopy

Transmission electron microscopy (TEM) observations of the nanopowder variants were made using high-resolution transmission electron microscopy (HRTEM) using an FEI Titan 80-300 operated at 200 kV. The nanopowder was first dispersed in isopropanol and placed in an ultrasonic bath for 15 minutes to reduce particle agglomeration. The nanopowder dispersed in this solution was then deposited by placing

a small droplet onto a holey carbon copper grid using a pipette. The copper grid containing the nanopowder was placed in a TEM sample holder and loaded into the TEM instrument. Bright-field TEM (BF-TEM) was used to gather information about the size and shape and to determine the structure and morphology of the nanopowder.

Thermal analysis

Thermogravimetric (TG) analysis was carried out on nanopowder and micro/nano bimodal powder samples using simultaneous thermal analyser STA 449 F1 Jupiter equipment (Simultaneous Thermal Analyser, Netzsch Thermal Analysis GmbH, Germany). Powder of required mass (500 mg for nanopowder and 2 g for bimodal powder) was loaded to an alumina crucible in the glove box. In the TG equipment, the samples were heated to 1350°C at a heating rate of 10°C/min, and the change in mass was recorded as a function of temperature. High purity hydrogen gas (99.9999%) was used with the aim of reducing the surface oxide early on during heating. A flow rate of 100 ml/min was maintained throughout the process.

Chemical analysis

The bulk carbon and oxygen levels of both powder and sintered compacts were determined using LECO TC-600 and LECO CS-844 instruments. The oxygen present in the sample reacted with the crucible, forming CO and CO₂. The CO and CO₂ amounts were measured by means of infrared (IR) sensors and used to estimate the amount of oxygen. To measure carbon, the sample was combusted in an induction furnace under the flow of oxygen. Based on the CO and CO₂ formed due to the reaction between carbon in the sample and oxygen, the amount of carbon in the sample was determined

Compaction and Sintering

Both variants of micro/nano bimodal powder were uniaxially compacted to cylindrical disks of 10 mm in diameter and 4 mm in height. Sintering was performed using a DIL 402C horizontal push rod dilatometer (Netzsch Thermal Analysis GmbH, Germany: DIL) under high purity hydrogen gas (99.9999%). A sintering temperature of 1250°C was employed at a heating rate of 10°C/min, followed by isothermal holding for 60 min at peak temperature and cooling to room temperature at a rate of 30°C/min. A sintering temperature of 1250°C is used in industrial setup for the sintering of ferrous powder when improved sintered density and mechanical performance are needed, which motivates the choice of maximum final temperature. For comparison, ASC 300 powder was compacted and sintered at the same temperature as that of the micro/nano bimodal powder compacts.

Optical microscopy

Optical microscopy was performed on mounted and polished sintered compacts containing carbon-coated nanopowder. This was performed to evaluate the fraction of pearlite using the Trainable Weka Segmentation tool, part of FIJI ImageJ freeware^{21 22}.

Scanning electron microscopy

High-resolution scanning electron microscopy (SEM) was performed using an LEO Gemini 1550 electron microscope (Carl Zeiss-LEO, equipped with a field emission gun: FEG-SEM) to evaluate the change in microstructure between sintered compacts containing iron nanopowder and carbon-coated iron nanopowder.

Density

The green density of the compacts was evaluated using a micrometer and a simple balance with an accuracy of 0.0001 g. The micrometer was used to measure the height and diameter of the cylinder and calculate the volume of the compact. The density of the sintered compacts was measured by means of the Archimedes principle. Porosity was assessed from optical micrographs taken at different locations with the aid of image analysis software and cross checked with the sintered density obtained from Archimedes principle measurements.

Hardness

Apparent hardness testing was performed using a Struers DuraScan 70G5 (Ballerup, Denmark) Vickers hardness tester at a 1 kg load on metallographic cross-sections of sintered compacts.

JMatPro

JMatPro 10.2 in conjunction with a general steel database was used to depict the phase fractions and phase transformations for the global alloy composition of the sintered materials studied.

Declarations

Acknowledgements

This work was carried out within the project 'Nanotechnology enhanced sintered steel processing' through support from Swedish Foundation for Strategic Research, SSF within the program 'Generic Methods and Tools for Future Production'. The authors would also like to acknowledge the support from 'Production Area of Advance', Chalmers University of Technology.

Author Contributions:

Conceptualization, methodology, investigation, data curation, formal analysis, writing—original draft and visualization, Swathi Manchili; investigation, data curation, formal analysis, Fang Liu; writing-review, editing and supervision, Eduard Hryha; writing—review, editing, supervision, project administration, and funding acquisition, Lars Nyborg. All authors have read and agreed to the published version of the manuscript.

The authors declare that they have no known competing financial interests or personal relationships that could have appeared to influence the work reported in this paper.

References

1. Höganäs. Material and powder properties. in *Höganäs handbook for sintered components* 86 (2013).
2. Oh, J. W., Seong, Y., Shin, D. S. & Park, S. J. Investigation and two-stage modeling of sintering behavior of nano/micro-bimodal powders. *Powder Technology* **352**, 42–52 (2019).
3. Manchili, S. K., Wendel, J., Hryha, E. & Nyborg, L. Sintering of bimodal micrometre/nanometre iron powder compacts - A master sintering curve approach. *Powder Technology* **391**, 557–568 (2021).
4. Choi, J.-P., Lyu, H.-G., Lee, W.-S. & Lee, J.-S. Densification and microstructural development during sintering of powder injection molded Fe micro–nanopowder. *Powder Technology* **253**, 596–601 (2014).
5. Edelstein, A. & Cammaratra, R. *Nanomaterials: synthesis, properties and applications*. (Institute of Physics Publishing, 1998).
6. Asoro, M. A., Kovar, D. & Ferreira, P. J. Effect of surface carbon coating on sintering of silver nanoparticles: In situ TEM observations. *Chemical Communications* **50**, 4835–4838 (2014).
7. Price, S. P., Henzie, J. & Odom, T. W. Addressable, Large-Area Nanoscale Organic Light-Emitting Diodes. *Small* **3**, 372–374 (2007).
8. Crone, B. *et al.* Electronic sensing of vapors with organic transistors. *Applied Physics Letters* **78**, 2229–2231 (2001).
9. Sun, G., Li, X., Wang, Q. & Yan, H. Synthesis of carbon-coated iron nanoparticles by detonation technique. *Materials Research Bulletin* **45**, 519–522 (2010).
10. Manchili, S. K. *et al.* Effect of Nanopowder Addition on the Sintering of Water-Atomized Iron Powder. *Metallurgical and Materials Transactions A* **50**, 4890–4901 (2020).
11. Díaz, J., Paolicelli, G., Ferrer, S. & Comin, F. Separation of the and components in the C1s photoemission spectra of amorphous carbon films. *Physical Review B - Condensed Matter and Materials Physics* **54**, 8064–8069 (1996).
12. Aarva, A., Deringer, V. L., Sainio, S., Laurila, T. & Caro, M. A. Understanding X-ray Spectroscopy of Carbonaceous Materials by Combining Experiments, Density Functional Theory, and Machine Learning. Part I: Fingerprint Spectra. *Chemistry of Materials* **31**, 9243–9255 (2019).
13. Luo, P., Nieh, T. G., Schwartz, A. J. & Lenk, T. J. Surface characterization of nanostructured metal and ceramic particles. *Materials Science & Engineering A* **5093**, 59–64 (1995).
14. Manchili, S. K. *et al.* Surface analysis of iron and steel nanopowder. *Surface and Interface Analysis* **50**, 1083–1088 (2018).
15. Manchili, S. K., Wendel, J., Hryha, E. & Nyborg, L. Analysis of iron oxide reduction kinetics in the nanometric scale using hydrogen. *Nanomaterials* **10**, 1–17 (2020).
16. Wendel, J., Manchili, S. K., Cao, Y., Hryha, E. & Nyborg, L. Evolution of surface chemistry during sintering of water-atomized iron and low-alloyed steel powder. *Surface and Interface Analysis* 1–5 (2020).

17. Wendel, J., Manchili, S. K., Hryha, E. & Nyborg, L. Reduction of surface oxide layers on water-atomized iron and steel powder in hydrogen: Effect of alloying elements and initial powder state. *Thermochimica Acta* **692**, 178731 (2020).
18. Hryha, E., Nyborg, L. & Alzati, L. Dissolution of carbon in Cr-prealloyed Pm steels: Effect of carbon source. *Powder Metallurgy* **58**, 7–11 (2015).
19. Oh, J. W., Seong, Y., Shin, D. S. & Park, S. J. Investigation and two-stage modeling of sintering behavior of nano/micro-bimodal powders. *Powder Technology* **352**, 42–52 (2019).
20. Sopinsky, M. V *et al.* Possibility of graphene growth by close space sublimation. *Nanoscale Research Letters* **9**, 182 (2014).
21. Arganda-Carreras, I. *et al.* Trainable Weka Segmentation: a machine learning tool for microscopy pixel classification. *Bioinformatics* **33**, 2424–2426 (2017).
22. Schindelin, J. *et al.* Fiji: an open-source platform for biological-image analysis. *Nature Methods* **9**, 676–682 (2012).

Figures

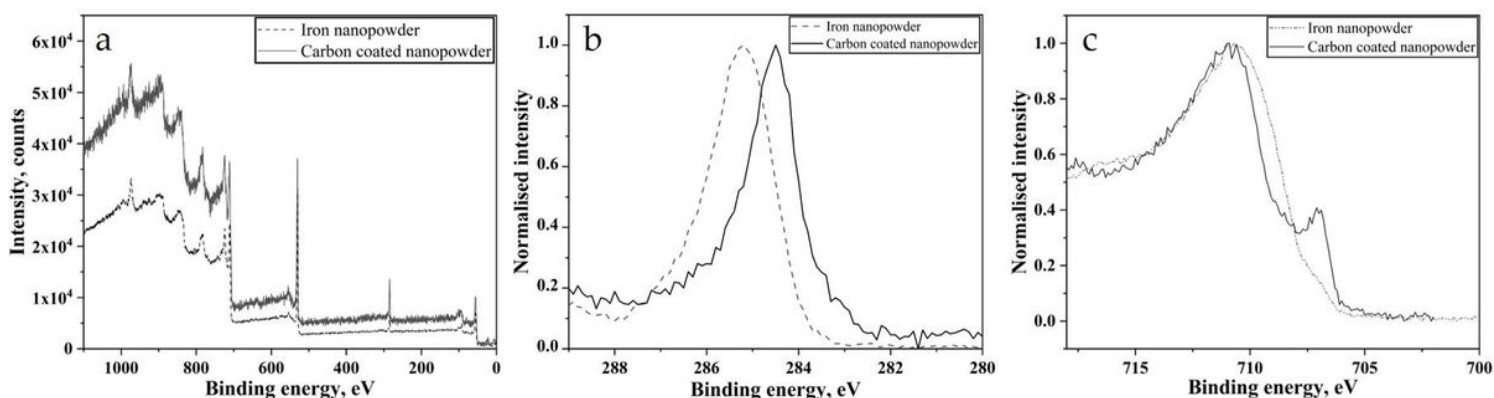


Figure 1

(a) XPS spectra recorded from the as-received surfaces of both nanopowder variants showing iron, oxygen and carbon peaks in the survey scan, (b) high-resolution XPS spectra for carbon (C1 s) from both variants showing the change in C1 s peak positions, and (c) high-resolution XPS spectra for iron (Fe2p^{3/2}) showing the presence of both oxide and metal iron peaks in both cases but with a higher relative intensity of metallic iron for the carbon-coated nanopowder.

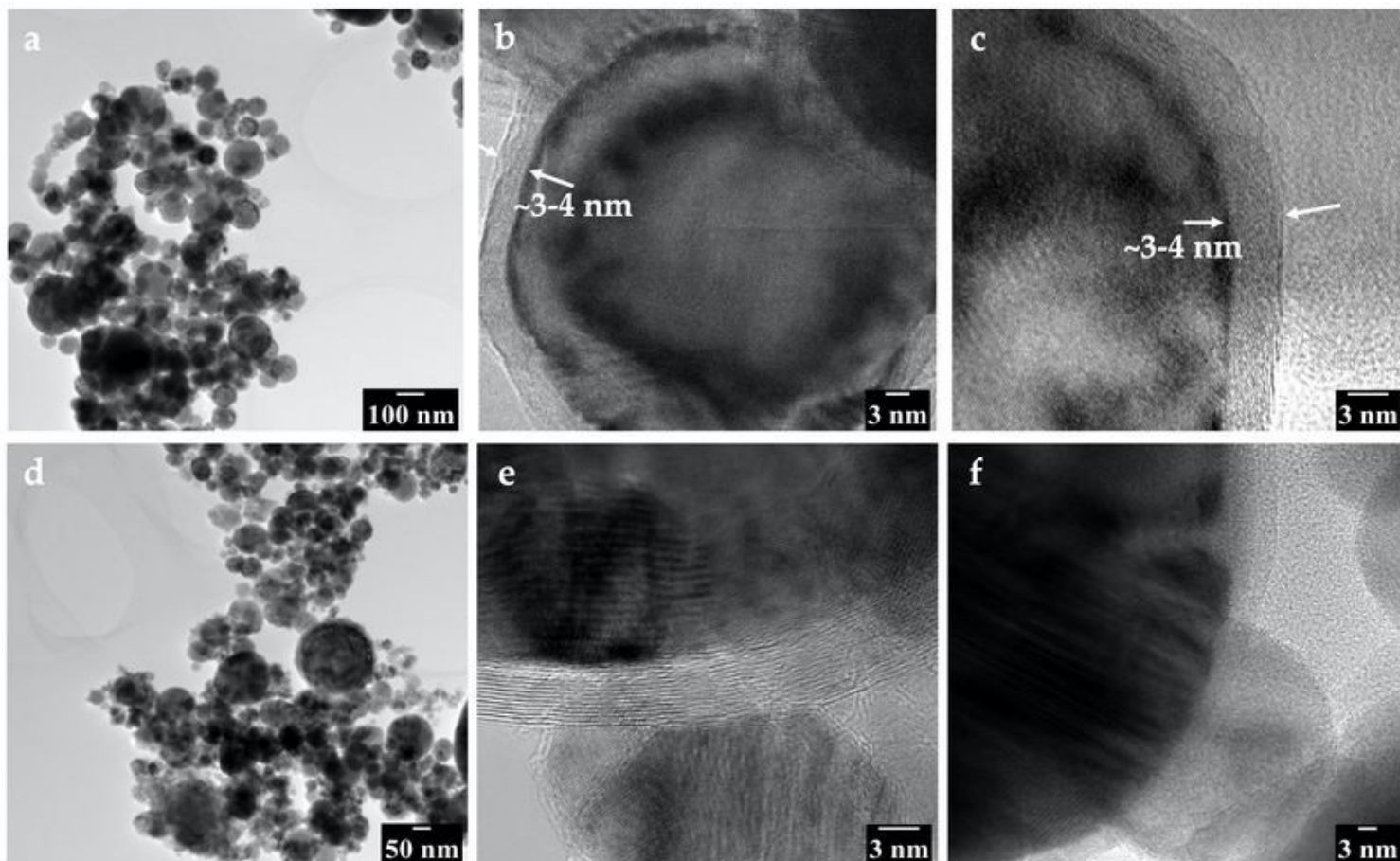


Figure 2

TEM images of iron nanopowder showing size and morphology of the particles (a), HRTEM images (b-c) revealing the surface oxide thickness, TEM images of carbon-coated iron nanopowder showing size and morphology of the particles (d) and HRTEM images (e-f) illustrating the core-shell structure with the iron core tightly coated with graphitic carbon layers.

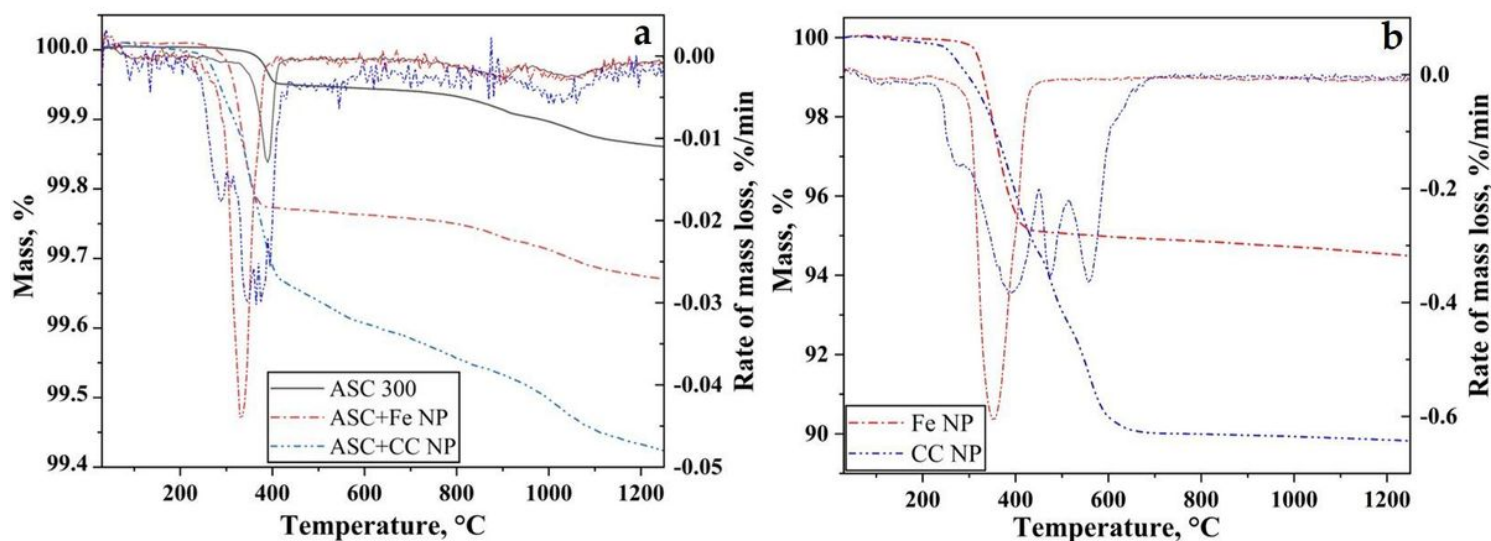


Figure 3

Thermogravimetry plots showing the change in mass and rate of mass change for (a) micrometer-sized powder without and with nanopowder additions and (b) for iron nanopowder and carbon-coated iron nanopowder alone.

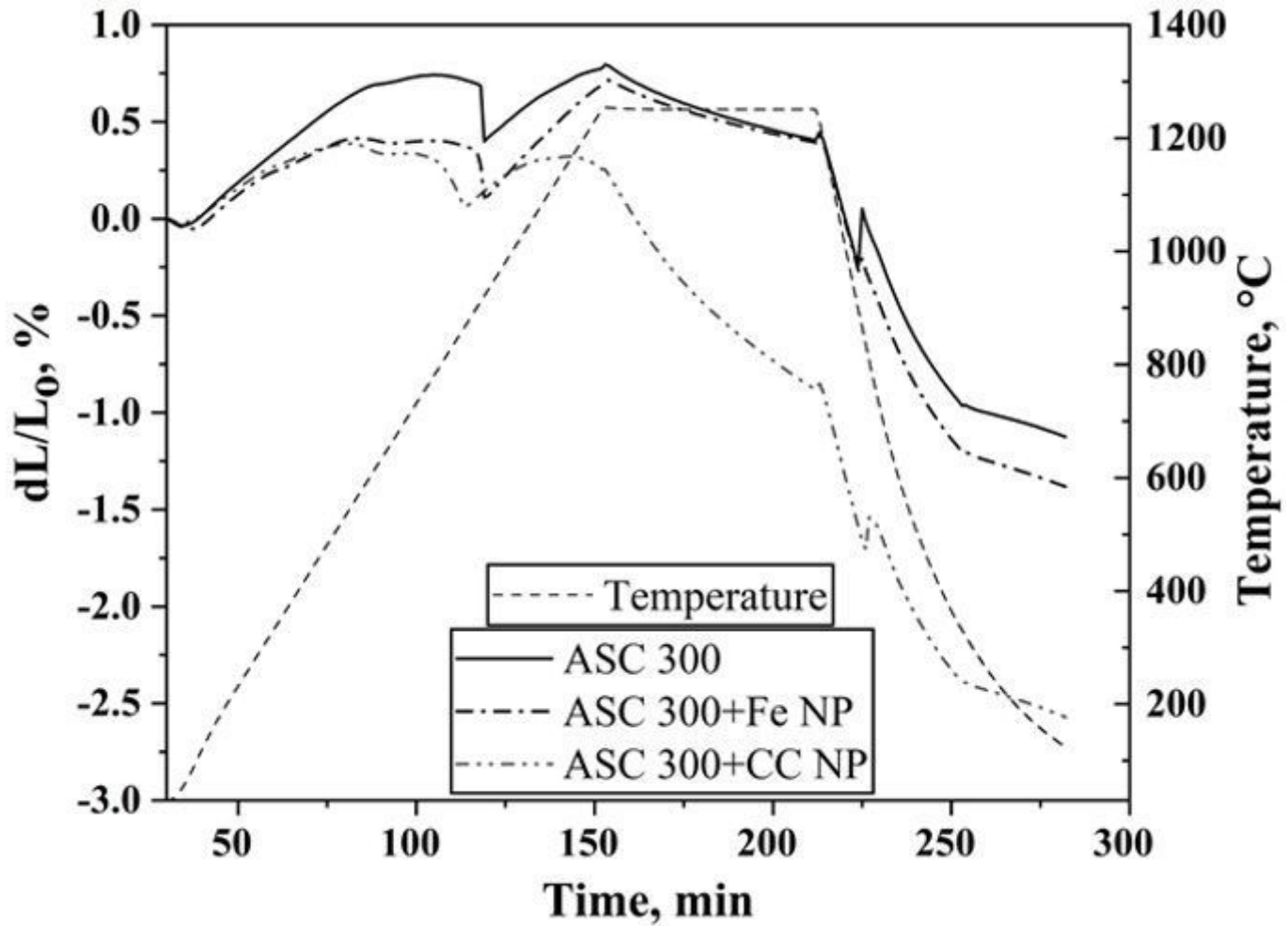


Figure 4

Sintering curves of ASC 300, ASC+Fe NPs and ASC+CC NPs at 1250 °C in pure hydrogen at a heating rate of 10 °C/min and a cooling rate of 30 °C/min.

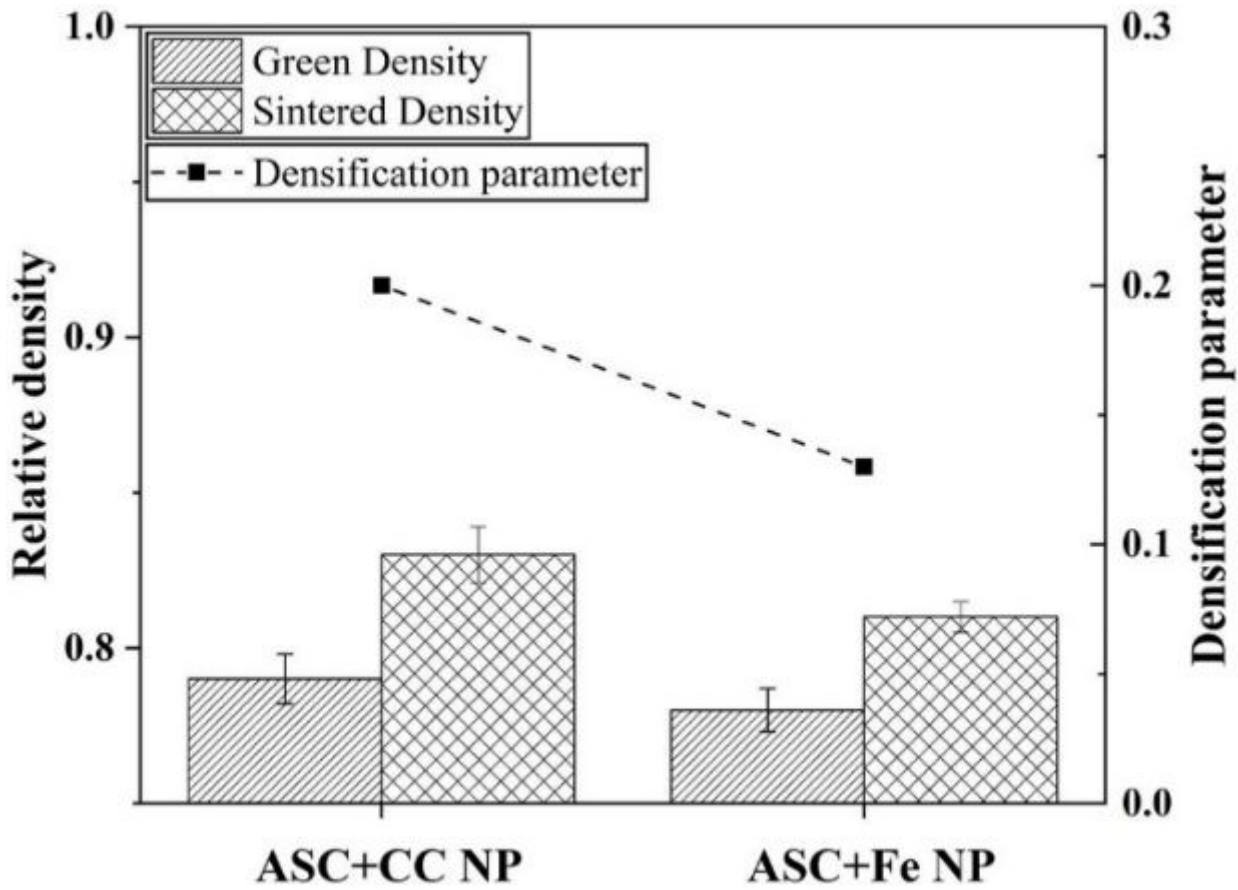


Figure 5

Green and sintered densities in relative terms of ASC+CC NP and ASC+Fe NP compacts along with densification parameters.

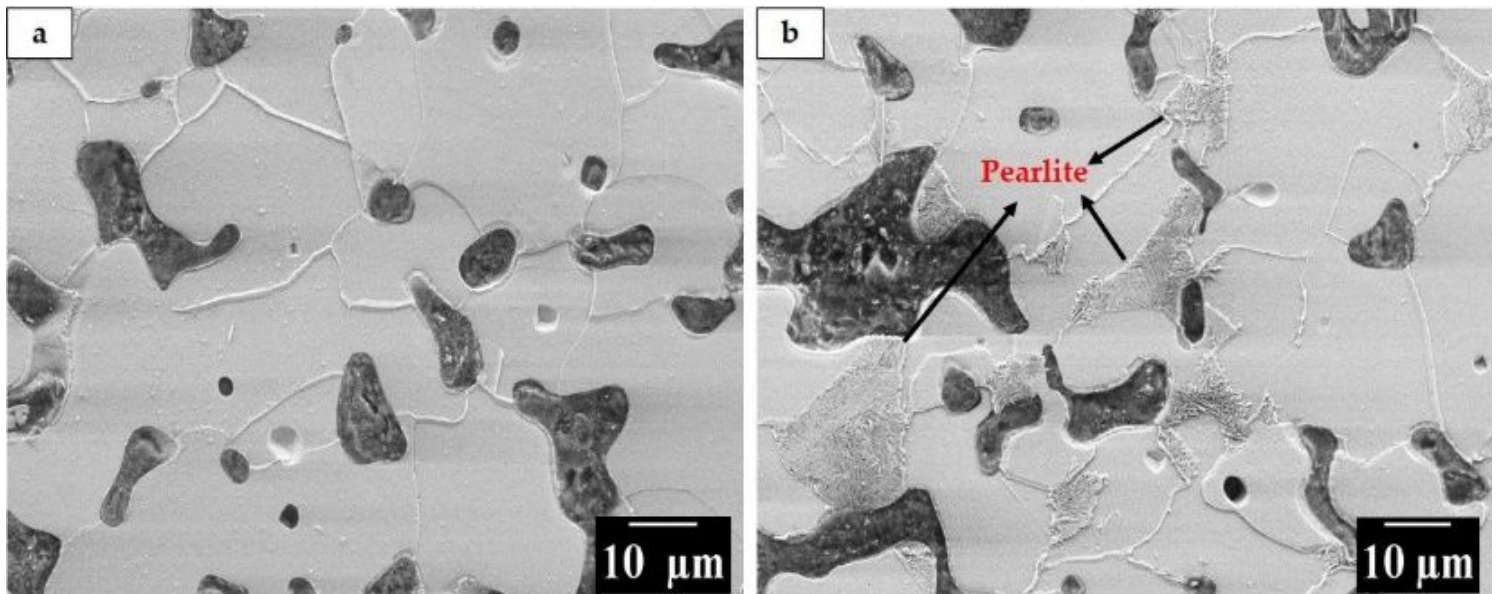


Figure 6

SEM micrographs of sintered compacts showing the microstructure of

ASC+Fe NP (a) and ASC+CC NP (b).

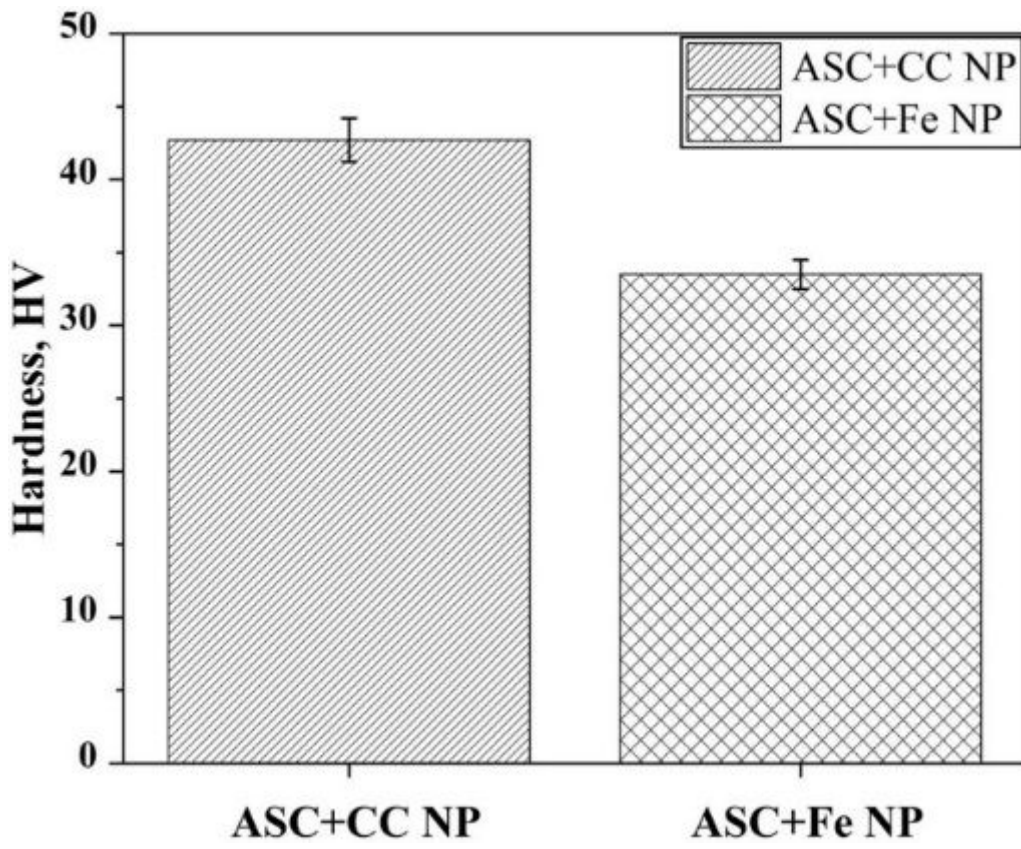


Figure 7

Plot showing the Vickers hardness of ASC+Fe NP and ASC+CC NP sintered compacts.